Journal of Power Sources 324 (2016) 342–348

Contents lists available at ScienceDirect

Journal of Power Sources

journal homepage: www.elsevier.com/locate/jpowsour

Effects of cathode electrolyte interfacial (CEI) layer on long term cycling of all-solid-state thin-film batteries

Ziying Wang [a], Jungwoo Z. Lee [a], Huolin L. Xin [b], Lili Han [b], Nathanael Grillon [c], Delphine Guy-Bouyssou [c], Emilien Bouyssou [c], Marina Proust [c], Ying Shirley Meng [a, *]

[a] Department of NanoEngineering, University of California, San Diego, La Jolla, CA 92093, USA
[b] Center for Functional Nanomaterials, Brookhaven National Laboratory, Upton, NY 11973, USA
[c] STMicroelectronics, CS 97155, 37071 Tours Cedex 2, France

HIGHLIGHTS

- Novel application of TEM analysis to interfaces in all-solid-state batteries.
- Discovery of an interfacial layer between LCO electrode and LiPON electrolyte.
- Analysis of interfacial impedance and capacity loss.
- Identification of interfacial growth mechanism.

GRAPHICAL ABSTRACT

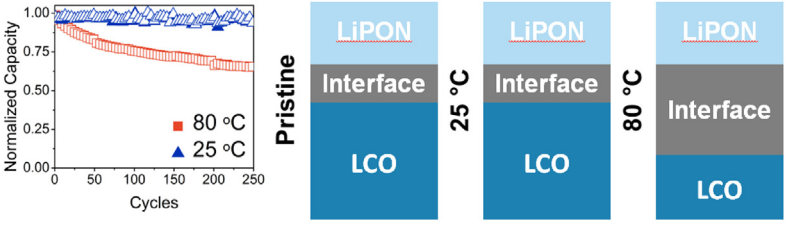

ARTICLE INFO

Article history:
Received 2 March 2016
Received in revised form
19 May 2016
Accepted 21 May 2016

Keywords:
Lithium-ion battery
Thin-film battery
Interfacial phenomena
Interface resistance
Solid electrolyte

ABSTRACT

All-solid-state lithium-ion batteries have the potential to not only push the current limits of energy density by utilizing Li metal, but also improve safety by avoiding flammable organic electrolyte. However, understanding the role of solid electrolyte – electrode interfaces will be critical to improve performance. In this study, we conducted long term cycling on commercially available lithium cobalt oxide (LCO)/lithium phosphorus oxynitride (LiPON)/lithium (Li) cells at elevated temperature to investigate the interfacial phenomena that lead to capacity decay. STEM-EELS analysis of samples revealed a previously unreported disordered layer between the LCO cathode and LiPON electrolyte. This electrochemically inactive layer grew in thickness leading to loss of capacity and increase of interfacial resistance when cycled at 80 °C. The stabilization of this layer through interfacial engineering is crucial to improve the long term performance of thin-film batteries especially under thermal stress.

1. Introduction

Lithium-ion batteries have become the focal point of energy storage devices as portable electronics and electric vehicles applications demand ever increasing energy densities both in terms of weight and volume. While the cost per Watt-hour of commercial batteries has decreased faster than expected due to high production and more efficient manufacturing [1], specific and volumetric energy densities have only increased 7–8% per year [2]. To truly relieve range anxiety, specific energy density higher than the current ~200 W h kg^{-1} is needed. To satisfy this demand, lithium-ion batteries utilizing solid state electrolytes show promise of a new paradigm shift in energy storage technologies. The introduction of solid state electrolyte could, in principle, yield many advantages over conventional lithium-ion batteries. Foremost, lithium metal can be used as the anode along with a high voltage cathode to boost

* Corresponding author. Department of NanoEngineering, University of California, San Diego, 9500 Gilman Drive, La Jolla, CA, USA.
E-mail address: shmeng@ucsd.edu (Y.S. Meng).

http://dx.doi.org/10.1016/j.jpowsour.2016.05.098
0378-7753/

energy density as the solid state electrolyte would prevent lithium dendrite formation. Secondly, removal of flammable liquid electrolytes greatly improves the inherent safety of the battery.

While thin-film lithium-ion batteries utilizing solid state electrolytes have begun to be commercialized in a variety of micro-devices such as radio-frequency identification tags, micro-electromechanical devices, sensors, and lab-on-a-chip systems [3,4], significant research on the chemical and electrochemical stability of the solid electrolyte – electrode interfaces is needed before big scale application in energy storage. Indeed, solid electrolyte – electrode interfacial resistance has now become the limiting factor in many systems [2]. Recent computational studies have shown that various interfaces are not always stable chemically or electrochemically leading to loss of capacity and increase in impedance [5,6]. Fortunately, thin-film batteries offer a convenient platform to investigate and gain insight into these interfacial phenomena due to their well defined geometry. The anode, electrolyte and cathode layers are clearly distinct over a large area, allowing for simplified analysis of various interfaces. Since the introduction of the first thin-film lithium-ion battery using the lithium cobalt oxide (LCO)/lithium phosphorus oxynitride (LiPON)/lithium (Li) chemistry [7,8], various reports have highlighted the role of LCO/LiPON interfacial resistance. Iriyama et al. has claimed that thermal treatment of the cell after LiPON deposition can reduce the interfacial resistance from 7925 Ω cm^2 to 125 Ω cm^2 [9,10]. Additionally, a recent paper by Haruta et al. has shown that an off-axis deposition of LiPON can greatly reduce the interfacial resistance down to 8.5 Ω cm^2 [11]. However, all these experiments were based on electrochemical measurements via electrochemical impedance spectroscopy (EIS) and did not identify the source of impedance.

In this study, we used Scanning Transmission Electron Microscopy (STEM) and Electron Energy Loss Spectroscopy (EELS) analysis to study the LCO and LiPON interface in commercially available LCO/LiPON/Li cells. When these cells were cycled at an elevated temperature of 80 °C, we observed continuous capacity decay and an increasing interfacial resistance contrasting stable cycling at 25 °C. Through TEM analysis of the LCO/LiPON interface, we were able to observe a distinct disordered LCO layer between the ordered LCO bulk and LiPON inherent to the solid electrolyte – electrode interface. The growth of this layer during high temperature cycling caused increasing interfacial resistance between LCO and LiPON as observed by electrochemical impedance spectroscopy. These results indicate that proper engineering of the electrode/electrolyte interface is essential for long term cell performance.

2. Experimental

2.1. Sample preparation and electrochemical testing

The all-solid-state thin-film batteries used in this study were supplied by STMicroelectronics. The cells were composed of deposited LCO, LiPON, Li layers on a mica substrate. The LCO layer was 8 μm thick. The exact thicknesses of LiPON and Li layers are omitted for industrial purposes but were on the orders of a few microns. The cells were then encapsulated to prevent air exposure. The current collectors were platinum and copper for the cathode and anode, respectively. Deposition of LCO and LiPON layers were done via medium-frequency & radio-frequency sputtering, respectively, while Li was thermally evaporated. A schematic of the battery is shown in Fig. 1a. The specific details about the deposition process are omitted for industrial purposes. The packaged thin film

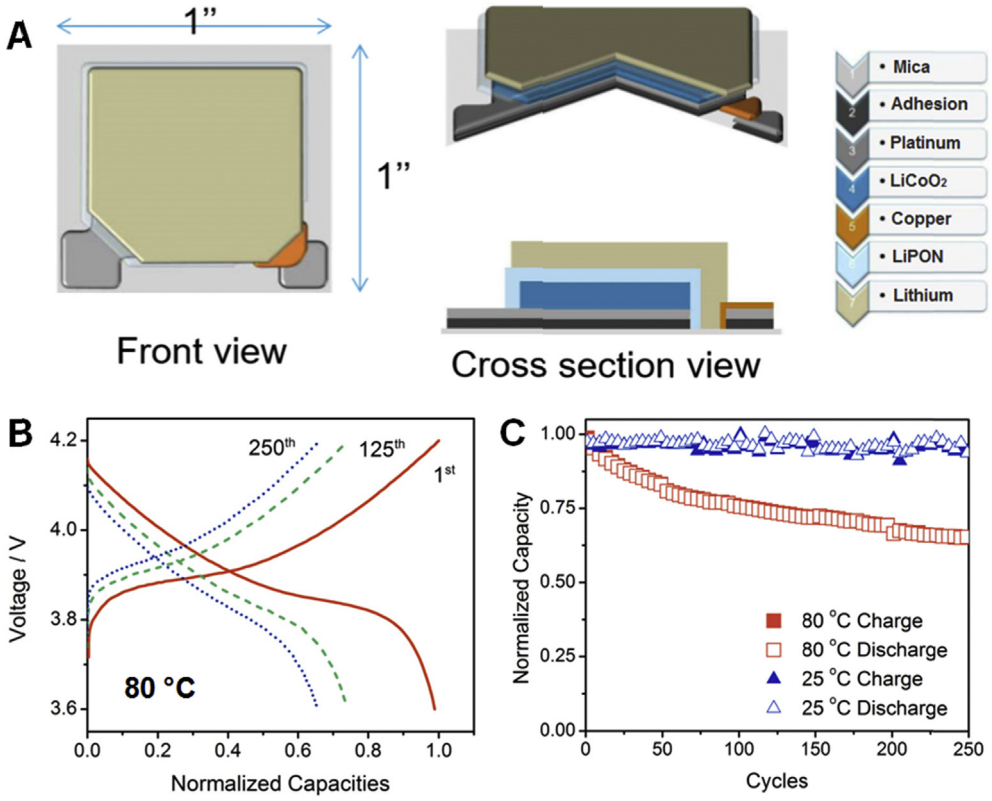

Fig. 1. a) Schematic of the thin-film battery. The all-solid-state thin-film battery consists of a lithium cobalt oxide (LCO) cathode, lithium phosphorus oxynitride (LiPON) electrolyte, and lithium anode. The cell is encapsulated to prevent air exposure. b) Cycling profile of the 80 °C cycled cell at 1st, 125th, and 250th cycle. c) Cycling capacity of the two cells over 250 cycles. The cell cycled at 80 °C quickly loses ~35% of its capacity over 250 cycles, while the cell cycled at 25 °C retains its capacity.

batteries had 1 inch × 1 inch footprint and were cycled with a rate of 1C at 25 °C or 80 °C via a potentiostat/galvanostat with a frequency response analyzer (Biologic SP-200). Electrochemical Impedance Spectroscopy (EIS) was conducted at room temperature every 50 cycles on each cell at the charged state. The frequency sweep was conducted from 1 MHz to 10 mHz with an amplitude of 10 mV and fitted with a complex non-linear least square fitting method. Two additional cells were aged at 60 °C for 2500 h without cycling. One cell was left in the discharged state at 3.6 V and the other was left in the charged state at 4.2 V after a single charge. The cells were then processed using a FEI Helios focused ion beam (FIB) to produce an *ex situ* cross section of the battery stack [12]. Subsequently, these samples were characterized in a JOEL 2100F analytical electron microscope with a 200 kV beam with an approximate energy resolution of 1 eV in electron energy loss spectra.

2.2. Scanning transmission electron microscopy collection

STEM-EELS images and spectrums were collected on a JEOL 2100F located at the Center for Functional Nanomaterials at Brookhaven National Laboratory. The beam energy was 200 kV. For all spectrums, the second smallest aperture was used where the beam density measured by the fluorescent screen was 2.4 pA cm^{-2}. The beam diameter was focused to approximately 0.2 nm. The energy resolution of the electron energy loss spectra was approximately 1 eV. For low loss mapping and spectrums, a 0.1 s pixel dwell time and 0.2 eV per channel dispersion were used. For high loss spectrums, a 20 s pixel dwell time, and 0.2 eV per channel dispersion were used. L_3/L_2 ratios were calculated by taking second derivative of the Co-L edge and comparing the height of the respective peaks for L_3 and L_2 in the second derivative. Selected area electron diffraction (SAED) was collected with the smallest objective aperture (~150 nm in diameter) to avoid diffraction from multiple layers. Focused Ion Beam processing of the samples were conducted on a FEI Helios nanolab. The maximum ion beam current used for regular cross sections is ~3 nA while the pixel dwell time was limited to 100 ns. The samples were extracted out of the full thin-film battery through typical lamella fabrication and thinned down to ~80 nm using 0.3 nA cleaning cross sections from both sides of the lamella.

2.3. Electron energy loss spectroscopy simulation by FEFF9

Electron energy loss spectroscopy simulations were conducted using FEFF9 software. The crystal structures of $LiCoO_2$, Li_2O, Li_2O_2, and LiO_2 were taken from icsd database for crystalline structures. The simulations were conducted using 200 keV beam energy, 10 mrad for collection and convergence angles. xkmax value of 4, xkstep value of 0.02, estep value of 0.01 were used. Hedin Lundqvist exchange and RPA corehole were used for electron core interactions.

3. Results and discussion

3.1. Cell cycling performance

Cycling profile of the thin-film battery cycled at 80 °C is shown in Fig. 1b. The cell was cycled between 3.6 V and 4.2 V and shows the characteristic voltage profile of the LCO intercalation reaction. Electrochemical curves show a plateau at approximately 3.9 V attributed to a first order phase transition between two hexagonal phases with different c lattice parameter due to the expansion of oxygen layer spacing [13,14]. The cell cycled at 80 °C lost ~35% of the original capacity over 250 cycles. In contrast, the cell cycled at 25 °C retained its capacity over the 250 cycles as seen in Fig. 1c. These charge/discharge characteristics show the distinctive behavior of batteries composed of LCO and confirm the good performance of the fabricated thin-film batteries.

3.2. TEM analysis

To fully understand the underlying mechanism of capacity decay, we used STEM-EELS characterization to locally probe the LCO/LiPON interface. Using standard FIB liftout techniques, three liftouts were made from the pristine, 25 °C, and 80 °C cycled samples, and thinned down to ~80 nm for TEM analysis, shown in Fig. 2a-c. It was observed that all three samples have an additional interfacial layer between LiPON and LCO. Close up TEM images of the cathode-electrolyte interfaces that more clearly distinguish the interfacial layers are shown in Fig. 2d-f. The imaging contrast between this additional layer and LCO is small as both layers are made of similar chemical compositions. This is confirmed by analysis of EELS taken from the interfacial layer, bulk LCO, and LiPON, both the interfacial layer and bulk LCO contain lithium, cobalt, oxygen but not phosphorus (Fig. S1). However, structural and chemical bonding differences between the interfacial layer and bulk LCO are drastic. Firstly, selected area electron diffractions conducted on the interfacial layers of all three samples did not show diffraction patterns that would originate from highly crystalline layered lithium cobalt oxide particles (Fig. 3a-c), contrasting clear polycrystalline diffraction rings from the bulk LCO layer (Fig. 3d). Radial integration of the diffraction patterns comparing between the pristine, 25 °C cycled, and 80 °C cycled samples (Fig. S2) shows that the interfacial layer contains highly disordered material. Weak diffraction signals from the pristine and 25 °C cycled samples align with reciprocal spacing of CoO rocksalt indicating that the interfacial layer contains a disordered rocksalt like cobalt oxide phase; while diffraction signals from the 80 °C align with reciprocal spacing of Li_2O. These results suggest that during cycling at elevated temperatures, a portion of the lithium and oxygen in the interfacial layer formed crystalline Li_2O along with the disordered cobalt oxide. Hereinafter, this interfacial layer and bulk LCO will be referred to as the disordered LCO and ordered LCO layers, respectively.

Comparing the 25 °C and 80 °C cycled samples (Fig. 2b-c), it is very apparent that the disordered layer has grown significantly at higher temperatures and has consumed approximately 4 μm of the cathode thickness. It is hypothesized that such growth will decrease the overall capacity of the cell. Without the proper layered oxide structure in the disordered layer, lithium-ions cannot be stored reversibly. However, due to the disordered nature of this interfacial layer, lithium conduction is still possible via percolation through channels that could arise in regions with lithium excess stoichiometry, as proposed by Lee et al. [15].

3.3. STEM-EELS analysis

It is important to probe the chemical bonding of elements in the disordered and ordered layers to analyze the local environment of atoms. Bonding between lithium, cobalt and oxygen atoms can have a large effect on the occupancy and energy of their electronic orbitals, which in turn can be characterized by electron energy loss spectroscopy (EELS). Low loss electron energy loss spectra taken from the three samples are shown in Fig. 4a. As the Li-K edge and Co-M edge are close in energy value and highly convoluted together, they must be analyzed together in low loss spectra. In the ordered LCO layer of all three samples, the low loss edges show peak shape corresponding to spectrum taken from crystalline lithium cobalt oxide standards. A supporting figure

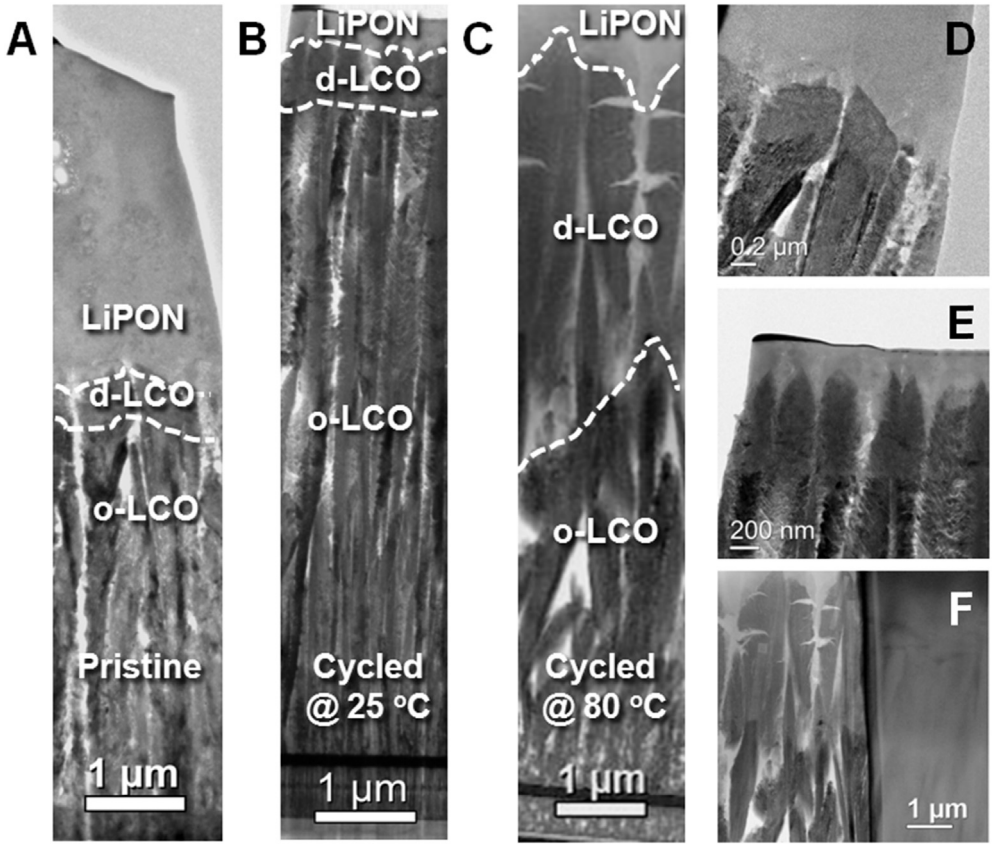

Fig. 2. Cross-sectional TEM images of the thin-film battery showing the cathode/electrolyte interface. a) pristine LCO/LiPON interface showing ~300 nm thick disordered layer. b) 25 °C cycled LCO/LiPON interface showing minimal change to the disordered layer. c) 80 °C cycled LCO/LiPON interface showing significant growth of the electrochemically inactive disordered layer. Close up TEM images of the cathode/electrolyte interface for the pristine, 25 °C, and 80 °C samples are shown in d)-e) respectively.

combining low loss and high loss spectra taken from the main samples and standards are shown in Fig. S3 for visual comparison but omitted in the main manuscript for visual clarity. There are small but subtle differences of the low loss edges from the disordered LCO layers. In the pristine and 25 °C cycled sample, the low loss edge contains a sharp peak ~60 eV resembling spectrum taken from crystalline cobalt oxide rocksalt standard (Fig. S3a). However in the 80 °C cycled sample, there is a much stronger edge shoulder before the onset of the main edge and this peak shape is seen previously in low loss EELS of Li_2O standards [16]. These results compliment our earlier observation of disordered rocksalt like cobalt oxide in the disordered layer of pristine and 25 °C samples and presence of Li_2O in the disordered layer of 80 °C sample.

Additionally, the O–K edge is very indicative of how the oxygen atom bonds to surrounding cations such as cobalt or lithium [17–20]. O–K edge spectra taken from the disordered and ordered layer of the three samples are shown in Fig. 4b; and as expected, all three spectra from the ordered layer show characteristic O-K pre-edge corresponding to hybridization of Co 3d and O 2p orbitals in LCO (Fig. S3b). However in the pristine cell, the O-K pre-edge in the disordered layer is already absent as compared to the ordered layer. This implies that in these particular samples, the Co-O hybridization bonding has already converted to a more ionic bond even in the pristine state. While there was no significant difference between the disordered layer of pristine and 25 °C sample, the O–K edge of the disordered layer in the 80 °C cycled sample shows a doublet peak with an approximately 5eV of energy spacing. From EELS simulations using FEFF9 of the O–K edge based on lithium oxide and lithium peroxide (Fig. S4), we see that the O–K pre-edge shifts to a higher energy level of ~535 eV which is consistent with the observed spectra of the 80 °C sample.

Electron energy loss spectra of transition metal L-edge also allow quantitative analysis of the oxidation state of transition metal cations. In Fig. 4c, the Co-L edges clearly show a shift of L_3 and L_2 edges to a lower energy level by about 1 eV in all three disordered LCO layers. Such shift is associated with transition metal cations of lower oxidation states (Fig. S3c). A more quantitative probing of the oxidation state can be obtained by calculating the L_3/L_2 ratio. Shown in Fig. 4d, the L_3/L_2 ratio of cobalt within the ordered LCO layer remains mostly constant near ~2.2 corresponding to Co^{3+} in $LiCoO_2$. The L_3/L_2 ratio of cobalt within the disordered LCO layer, however, becomes slightly lower after cycling and much lower after cycling at 80 °C. Based on L_3/L_2 ratio calculated from $LiCoO_2$, Co_3O_4, and CoO standards, the average oxidation states of cobalt in the disordered layer of pristine, 25 °C, and 80 °C samples are estimated to be 2.1+, 2.2+, and 2.5 + respectively. Oxidation state of cobalt provides clues to the underlying mechanism of the formation and growth of the disordered layer.

3.4. Mechanism of disordered layer formation and growth

The disordered LCO layer is present in the pristine sample indicating that the pairing of LiPON electrolyte and $LiCoO_2$ cathode has an inherent chemical instability leading to formation of a decomposition layer. This chemical instability is also observed via theoretical computations of thermodynamic energies of decomposition products [5,21]. After the deposition of LiPON, ~300 nm of the $LiCoO_2$ cathode film surface decompose to form a highly disordered rocksalt like cobalt oxide material as evidenced by SAED

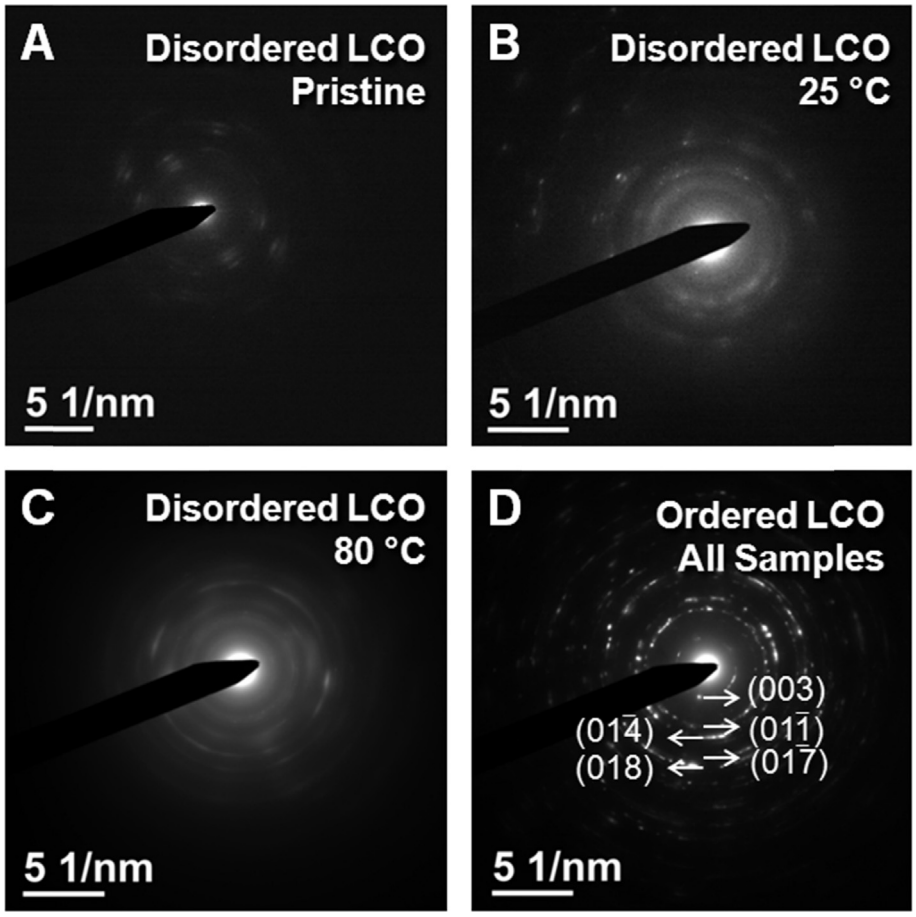

Fig. 3. Selected area electron diffractions taken from the disordered LCO layer of the pristine, 25 °C, 80 °C samples are shown in a)-c). The disordered layers all show highly disordered diffraction rings while the ordered LCO layer show highly crystalline diffraction rings corresponding to layered oxide crystal structure as shown in d).

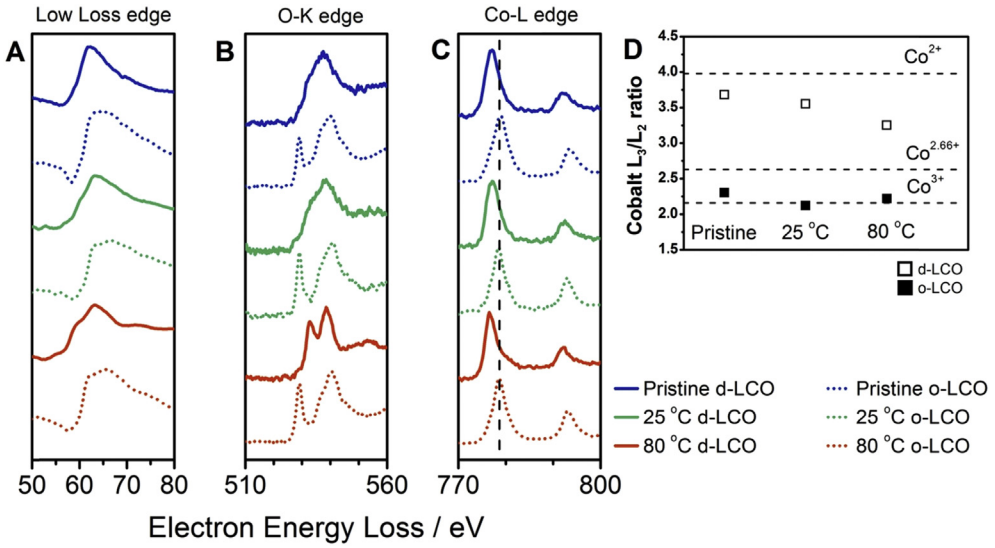

Fig. 4. Electron energy loss spectra taken from all three samples. A) Low loss Li-K/Co-M edges, B) O-K edges, and C) Co-L edges taken from the disordered and ordered LCO layers of the pristine, 25 °C, and 80 °C samples. All the spectra taken from the ordered LCO layers show characteristic peak shapes and energies for crystalline $LiCoO_2$. Low loss Li-K/Co-M edges in the disordered LCO layer show subtle differences in the edge shoulder between the 25 °C and 80 °C sample and O–K edges show a doublet peak with 5 eV spacing in the disordered LCO layer of the 80 °C sample. Both peak shapes can be attributed to Li_2O formation. All Co-L edges from the disordered LCO layer are shifted to a lower energy level indicating reduction of cobalt. Calculated Co L3/L2 ratios from the disordered and ordered LCO layers of all three samples are shown in D).

and EELS analysis. Cobalt ions within this decomposition layer are reduced to an average oxidation state of 2.1+ from 3+ through the formation of peroxide species. However, due to relatively weak intensity of O–K pre-edge in Li_2O_2 FEFF9 simulation (Fig. S4), only a

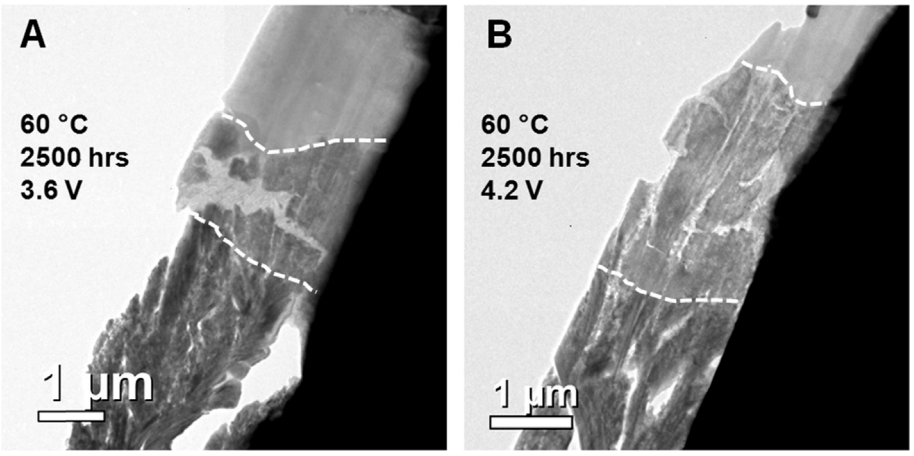

Fig. 5. TEM images of cells aged at 60 °C for 2500 h. One cell was kept in the discharged state (3.6 V) shown in a) while another cell was kept in the charged state (4.2 V) shown in b). The disordered LCO layer grew to about 1.5 μm in thickness in the discharged sample and about 3 μm in thickness in the charged sample.

single peak is observed for the O–K edge in both the pristine and 25 °C samples. In addition to the initial chemical decomposition, the disordered LCO layer can continue to grow into the ordered LCO layer through a combination of thermal and electrochemical activation to form a different decomposition phase that contains more Li_2O and trivalent cobalt. It's important to first note that electrochemical activation alone does not promote the growth of the disordered LCO layer. As can be seen from the 25 °C cycled sample (Fig. 2b), there was no change to the thickness of the disordered layer after 250 cycles. To properly compare thermal effects alone and thermal effects with electrochemical bias, two additional cells were tested without cycling. One cell was kept in the discharged state at 3.6 V while the other was kept in the charged state at 4.2 V after a single charge, and both cells were then heated at 60 °C for 2500 h. TEM images of these two samples show that thermal activation alone was able to grow the disordered LCO layer to ~1.5 μm in the discharged sample (Fig. 5a), while the disordered LCO layer grew to an even thicker ~3 μm in the charged sample (Fig. 5b). Variation in thickness of the disordered LCO layer is most likely due to a combination of uneven surface morphology of the initial crystallized LCO cathode and small differences in local decomposition rate. From these two experiments, we can conclude that the main driving force for further decomposition is thermal activation and electrochemical delithiation of $LiCoO_2$ enhances the rate of decomposition. Initial heat stress during RF sputtering of LiPON on LCO could have also contributed to the initial 300 nm thickness of disordered layer. Future experiments correlating fabrication conditions and initial composition and morphology of the disordered layer could provide further insight to its formation mechanism.

Chemically, it is hypothesized that during high temperature cycling the disordered LCO layer grows through the decomposition of ordered LCO into disordered rocksalt like cobalt oxide, lithium oxide and lithium peroxide. The reduction of trivalent cobalt is charge balanced by formation of appropriate amounts of lithium peroxide. The decomposition reaction in the disordered LCO layer of 80 °C sample can be summarized in Equation (1) resulting in $Co^{2.5+}$ observed through Co L_3/L_2 analysis.

$$4LiCoO_2 \rightarrow Li_2O + Li_2O_2 + Co_4O_5 \quad (1)$$

3.5. Electrochemical impedance spectroscopy analysis

EIS conducted on the cell cycled at 80 °C provides additional insight into the changes of interfacial impedance that occurs during cycling. The impedance spectra taken at the charged state every 50 cycles are shown in Fig. 6a and show increasing interfacial impedance over 250 cycles. The impedance spectra consist of three semicircles, two in the high frequency range with characteristic frequencies of 77 kHz and 455 Hz and one in the low frequency range with characteristic frequency of 103 mHz. The first semicircle remains constant over the entire 250 cycles and is attributed to the ionic conduction of lithium-ions in LiPON. Given the geometry of the cell, the ionic conductivity of the LiPON is estimated

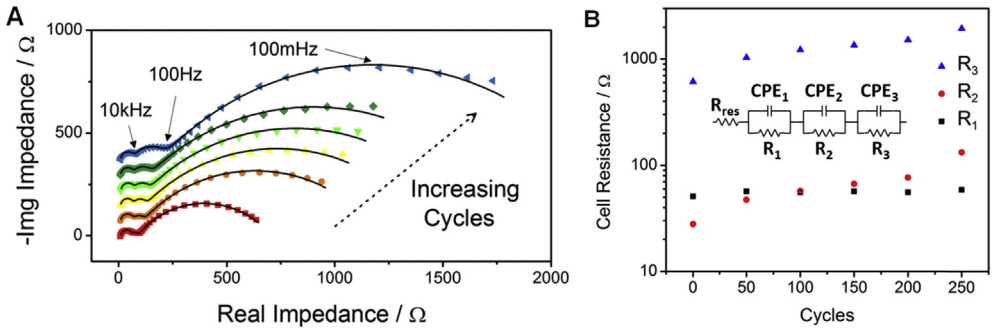

Fig. 6. a) Electrochemical impedance spectroscopy of the 80 °C cycled cell. The EIS spectra of the full cell taken every 50 cycles show that the interface impedance increases as the cell ages. b) The extracted values of charge transfer resistance of various processes in the full cell. R_1 is attributed to the ionic conductivity of LiPON. R_2 is attributed to the charge transfer resistance between the disordered LCO layer and LiPON while R_3 is attributed to the charge transfer resistance between the disordered LCO layer and ordered LCO layer.

to be 2.1 × 10^{-6} S cm^{-1} which agrees with literature values [22]. As seen from previous literature, the interfacial resistance between Li/LiPON is negligible compared to the other interfaces and will not be included in the fitting [9,11,23]. The second and third semicircles can be attributed to two different charge transfer processes, which steadily increase in resistance over 250 cycles. The fitted spectra using the equivalent circuit are presented in Fig. 6a, while Fig. 6b exhibits the evolution of each contribution over the 250 cycles. Detailed fitting parameters are shown in Supplementary Table 1.

Keeping the observation of the disordered layer in mind, we can precisely interpret the physical representations of the EIS data. When EIS was conducted on the electrochemical cell (Fig. S5) at the discharged state (3.6 V), we do not see a third semicircle as the electrochemical Li intercalation reaction between the ordered LCO layer and disordered LCO layer only occurs above ~3.9 V [9,10]. Hence, the second semicircle with a characteristic frequency of 755 Hz can be attributed to charge transfer resistance between the LiPON layer and the disordered LCO layer, while the third semicircle with a characteristic frequency of 103 mHz can be attributed to charge transfer resistance between the disordered LCO layer and ordered LCO layer. As the disordered LCO layer grows in thickness upon cycling, its impedance at the LiPON and ordered LCO interfaces increases. It is also important to note that in the 25 °C cycled cell, the impedance spectra (Fig. S6) remain mostly unchanged over 250 cycles mirroring the lack of growth of the disordered LCO layer.

4. Conclusion

We used STEM-EELS and EIS to elucidate capacity decay mechanisms of commercial all-solid-state thin-film batteries. By cycling these all-solid-state batteries at elevated temperatures, we were able to measure a significant increase in interfacial resistance due to the growth of a disordered interphase layer, which grew from ~300 nm in the pristine state to over four microns after cycling at 80 °C. High temperature causes the decomposition of LCO into disordered rocksalt like cobalt oxide, Li_2O and Li_2O_2 while electrochemical cycling enhances the rate of decomposition. During cycling, the disordered layer consumes electrochemically active cathode layer, reducing the overall capacity. Through the combination of STEM-EELS and EIS, we were able to gain critical information correlating bulk scale performance and nanoscale probing. The analytical information gathered will help improve future engineering of all-solid-state batteries to establish new design rules for solid-solid interfaces and improve the electrochemical performance and lifetime of such devices.

Acknowledgment

We would also like to acknowledge the funding for the characterization of all-solid-state battery by the U.S. Department of Energy, Office of Basic Energy Sciences, under award number DE-SC0002357. The authors acknowledge the partial funding support and sample fabrication from STMicroelectronics. This research used resources of the Center for Functional Nanomaterials, which is a U.S. DOE Office of Science Facility, at Brookhaven National Laboratory under Contract No. DE-SC0012704.

Appendix A. Supplementary data

Supplementary data related to this article can be found at http://dx.doi.org/10.1016/j.jpowsour.2016.05.098.

References

[1] B. Nykvist, M. Nilsson, Nat. Clim. Change 5 (2015) 329–332.
[2] A.C. Luntz, J. Voss, K. Reuter, J. Phys. Chem. Lett. 6 (2015) 4599–4604.
[3] B. Fleutot, B. Pecquenard, F. Le Cras, B. Delis, H. Martinez, L. Dupont, D. Guy-Bouyssou, J. Power Sources 196 (2011) 10289–10296.
[4] V.P. Phan, B. Pecquenard, F. Le Cras, Adv. Funct. Mater. 22 (2012) 2580–2584.
[5] W.D. Richards, L.J. Miara, Y. Wang, J.C. Kim, G. Ceder, Chem. Mater. 28 (2016) 266–273.
[6] L.J. Miara, W.D. Richards, Y.E. Wang, G. Ceder, Chem. Mater. 27 (2015) 4040–4047.
[7] B. Wang, J.B. Bates, F.X. Hart, B.C. Sales, R.A. Zuhr, J.D. Robertson, J. Electrochem. Soc. 143 (1996) 3203–3213.
[8] J.B. Bates, N.J. Dudney, ASAIO J. 43 (1997) M647.
[9] Y. Iriyama, T. Kako, C. Yada, T. Abe, Z. Ogumi, J. Power Sources 146 (2005) 745–748.
[10] Y. Iriyama, T. Kako, C. Yada, T. Abe, Z. Ogumi, Solid State Ionics 176 (2005) 2371–2376.
[11] M. Haruta, S. Shiraki, T. Suzuki, A. Kumatani, T. Ohsawa, Y. Takagi, R. Shimizu, T. Hitosugi, Nano Lett. 15 (2015) 1498–1502.
[12] W. Ziying, M. Ying Shirley, Analytical electron microscopy study of all solid-state batteries, in: Handbook of Solid State Batteries, World Scientific, 2015, pp. 109–131.
[13] J.N. Reimers, J.R. Dahn, J. Electrochem. Soc. 139 (1992) 2091–2097.
[14] T. Ohzuku, A. Ueda, J. Electrochem. Soc. 141 (1994) 2972–2977.
[15] J. Lee, A. Urban, X. Li, D. Su, G. Hautier, G. Ceder, Science 343 (2014) 519–522.
[16] F. Wang, J. Graetz, M.S. Moreno, C. Ma, L. Wu, V. Volkov, Y. Zhu, ACS Nano 5 (2011) 1190–1197.
[17] J. Graetz, A. Hightower, C.C. Ahn, R. Yazami, P. Rez, B. Fultz, J. Phys. Chem. B 106 (2002) 1286–1289.
[18] S. Stemmer, A. Sane, N.D. Browning, T.J. Mazanec, Solid State Ionics 130 (2000) 71–80.
[19] M.K. Aydinol, A.F. Kohan, G. Ceder, K. Cho, J. Joannopoulos, Phys. Rev. B 56 (1997) 1354–1365.
[20] G. Ceder, A.V.d. Ven, C. Marianetti, D. Morgan, Model. Simul. Mater. Sci. Eng. 8 (2000) 311–321.
[21] Y. Zhu, X. He, Y. Mo, J. Mater. Chem. A 4 (2016) 3253–3266.
[22] J.B. Bates, N.J. Dudney, G.R. Gruzalski, R.A. Zuhr, A. Choudhury, C.F. Luck, J.D. Robertson, Solid State Ionics 53 (1992) 647–654.
[23] D.G.-B.S. Larfaillou, F. Le Cras, S. Franger, in: ECS Meeting, Orlando, 2014.